Supporting information for: Circular swimming motility and disordered hyperuniform state in an algae system

Mingji Huang,[1] Wensi Hu,[2] Siyuan Yang,[1] Quan-Xing Liu,[2,3] and H. P. Zhang[1,4,*]

[1] *School of Physics and Astronomy and Institute of Natural Sciences, Shanghai Jiao Tong University, Shanghai, China*
[2] *State Key Laboratory of Estuarine and Coastal Research, School of Ecological and Environmental Sciences, East China Normal University, Shanghai 200241, China*
[3] *Shanghai Key Lab for Urban Ecological Processes and Eco-Restoration & Center for Global Change and Ecological Forecasting, School of Ecological and Environmental Sciences, East China Normal University, Shanghai 200241, China*
[4] *Collaborative Innovation Center of Advanced Microstructures, Nanjing, China*

(Dated: March 31, 2021)

I. INDIVIDUAL CELL MOTILITY

A. Diurnal motility pattern

We culture *E. voratum* under periodic illuminations, with 12-hour light-on and 12-hour light-off. During the 24-hour cycle, we measured the ratio of actively swimming cells in population every 3 hours. Results in Fig. S1 clearly shows a 24-hour diurnal pattern for cell motility [1]. Percentage of motile cells at the bottom solid-liquid interface reaches a maximal value about 8 hours after the light is turned on. Our experiments are carried out during the period of 8-12 hours after the light is turned on.

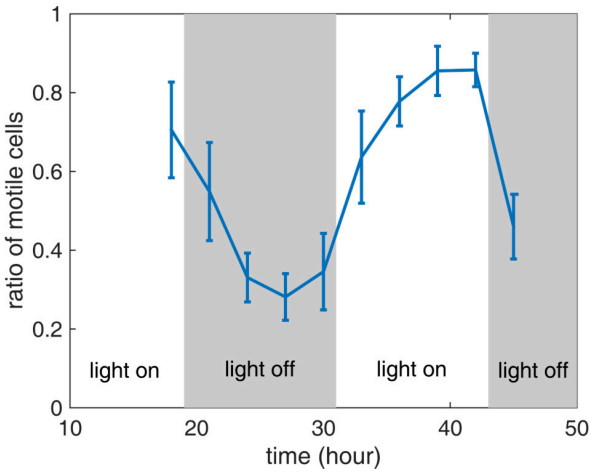

Figure S1. Ratio of motile cells on the liquid-glass interface at different phases of diurnal cycles. Error-bars represent variations among 12 different samples.

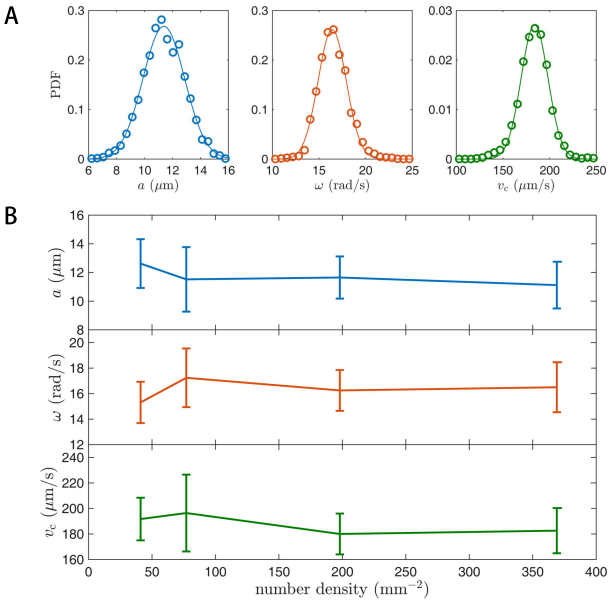

Figure S2. (A) Probability distribution functions of radius, angular and linear speed of circular cell motions in a sample with a density of 198 mm^{-2}. (B) Mean and standard deviation of these three quantities in samples with cell density of 41, 77, 198, and 369 mm^{-2}.

B. Distribution of motility characteristics

We quantify circular cell motion, cf. Fig. 1*C*, by its radius, angular and linear speed. Probability distribution functions of these three quantities in a sample with a density of 198 mm^{-2} are shown in Fig. S2*A*. All distributions can be fitted by a normal distribution, from which we extract the mean and standard deviation. In Fig. S2*B*, we plot the mean and standard deviation extracted from different samples. Results are approximately independent of cell density; the mean values for radius, angular and linear speed are 11.6 μm, 16.2 rad/s, and 180 μm/s, respectively.

* hepeng_zhang@sjtu.edu.cn

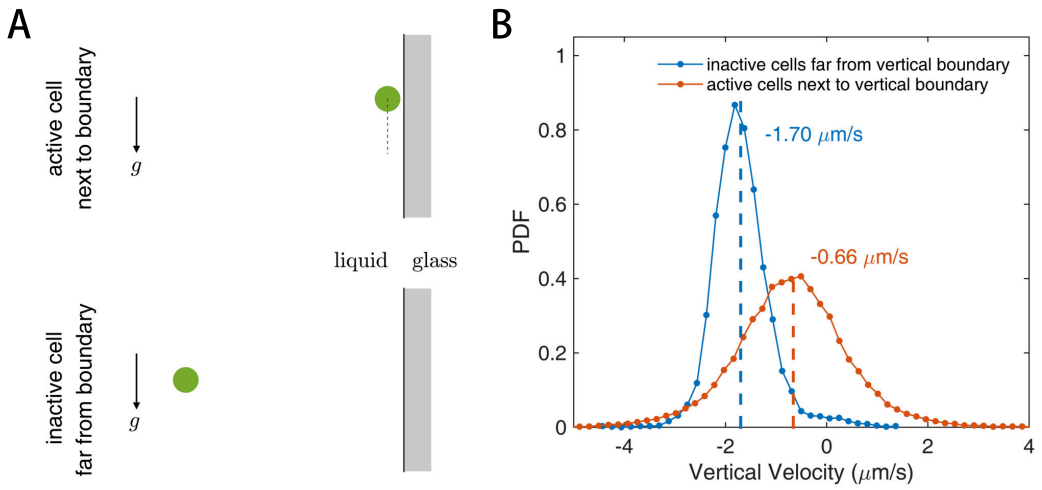

Figure S3. (A) Schematic illustrations of a cycling cell segmenting close to a vertical wall and of a dead cell sedimenting far away from a wall. (B) Distribution of sedimenting velocities in these 2 cases.

C. Gap between cell and interface

To quantitatively reproduce measured flow field in Fig. 2*A*, we need to know the gap between the cycling cell and the interface. For that, we measure sedimentation speed of cycling cells near a vertical liquid-glass interface, and compare the result to sedimentation speed of dead cells in the bulk fluid, cf. Fig. S3*A*. Probability distribution functions of two quantifies are shown in Fig. S3*B*. Cells sediment significantly slower near the interface: $\langle U\rangle = 0.66$ μm/s and $\langle U_\infty\rangle = 1.70$ μm/s; this is presumably caused by the increase of hydrodynamic drag near a no-slip boundary [2]. We assume swimming of cycling cells doesn't affect its sedimentation over a long distance and treat the cell as a passive sphere with a radius of $R_{\rm cell}$. Under these assumption, Low-Reynolds number hydrodynamic theory predicts the ratio of two sedimentation speeds is determined as follows [2]:

$$\frac{\langle U\rangle}{\langle U_\infty\rangle} = 1 - \frac{9}{16}\frac{R_{\rm cell}}{l} + \frac{1}{8}\left(\frac{R_{\rm cell}}{l}\right)^3 - \frac{45}{256}\left(\frac{R_{\rm cell}}{l}\right)^4 - \frac{1}{16}\left(\frac{R_{\rm cell}}{l}\right)^5, \tag{S1}$$

where l is the distance from the sphere center to the boundary. From this equation and measured sedimentation speeds, we have $R_{\rm cell}/l = 0.943$. For a cell of radius $R_{\rm cell} = 5.0$ μm, we have $l = 5.3$ μm, which leads to a gap of 0.3 μm.

D. Non-circular motion and flagellar dynamics

Fig. S4 shows how a cell transits from circular to non-circular motion at the air-liquid interface. In the first half second (0-0.5 s), the cell follows a circular trajectory and its longitudinal flagellum beating at the normal (side-way) position, as shown in Fig. S4*B*. However, starting at three instants (0.55 s, 0.75 s, and 1.00 s), the cell swims linearly and the longitudinal flagellum extends to the backside of the cell. This shows that the transition between circular and non-circular motion is strongly correlated to the beating position of the longitudinal flagellum, which is possibly controlled by noises in flagellar oscillation [3–5].

E. Statistics of non-circular motion

The transition from circular to non-circular motion can be identified by the following procedure from instantaneous cell position, $\boldsymbol{r}(t)$. Taking the trajectory in Fig. S5*A* as an example, we first compute the tangential and normal components of the cell acceleration from $\boldsymbol{r}(t)$, then project the trajectory onto a phase-plane of these two acceleration components, which are normalized by their respective standard deviations. As shown in Fig. S5*B*, data points corresponding to circular motion are clustered inside a dashed circle in the plane and those from non-circular motion significantly deviate from the circular values, i.e. outside of the circle. Quantitatively, we plot the acceleration deviation from the circular value (center of the dash circle) as a function of time in the lower panel of Fig. S5*C*. A cell is considered to be in circular motion if its acceleration deviation remains below a threshold of 6 for at least 0.4 sec; the period between two adjacent circular motion phases is considered to be non-circular if cells travel more than 30 μm (approximately the circular "donut" diameter, cf. Fig. 3*A*) during the period. Circular and non-circular phases, identified by the above procedure, are colored in blue and orange in

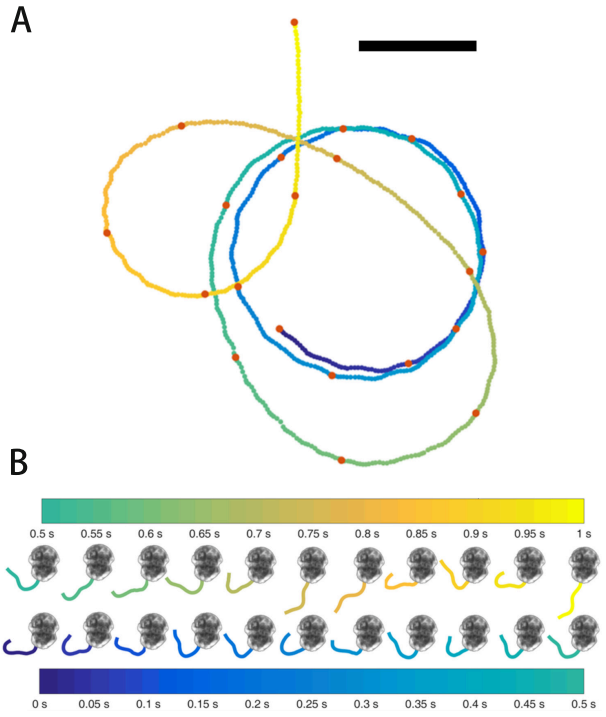

Figure S4. Transition from circular to non-circular motion. (A) Cell trajectory for one second. Color code represents time. Cell positions at every 0.05 s are marked by red points; shapes of the longitudinal flagellum at these marked positions are shown in (B).

Fig. S5*A*-*C*, respectively.

We apply the above procedure to a data set obtained at cell density of 198 mm^{-2}, which is 900 sec long and contains 4855 cell trajectories; 5137 events of non-circular motion are identified. This means that, on average, non-circular motion occurs to a cell at a rate of 1.2×10^{-3} s^{-1}. Probability distributions of temporal duration and spatial displacement of non-circular motion are plotted in Fig. S5*D*-*E*, which show a power-law scaling with an exponent of -3 for large values. Fig. S5*D* also shows that non-circular motion lasts less than 10 sec, which is the typical time step in particle-based simulations; thus, in simulations, we assume that non-circular motion occurs in a single time step, see main text for details. Green dashed line in Fig. S5*E* represents the distribution of non-circular motion distance produced by our model, using parameters corresponding to cell density of 198 mm^{-2} in Table SIII.

II. HYDRODYNAMIC MODEL

A. Method of regularized Stokeslets

In the method of regularized Stokeslets, fluid flow around a swimmer is generated by N localized forces $\boldsymbol{f}^{(i)}$ at $\boldsymbol{r}^{(i)} = \left(x^{(i)},\ y^{(i)},\ z^{(i)} \right)^{\mathrm{T}}$ on the swimmer surface:

$$\boldsymbol{v}\left(\boldsymbol{r}\right) = \sum_{i=1}^{N} \boldsymbol{S}\left(\boldsymbol{r}-\boldsymbol{r}^{(i)}\right)\boldsymbol{f}^{(i)}, \tag{S2}$$

where $\boldsymbol{S}\left(\boldsymbol{r}\right)$ is the regularized Green's function for the velocity [6, 7]. To guarantee the free-slip boundary condition at the interface $z = 0$, $\boldsymbol{S}\left(\boldsymbol{r}\right)$ includes the contributions from the localized force at $\boldsymbol{r}^{(i)} = \left(x^{(i)},\ y^{(i)},\ z^{(i)} \right)^{\mathrm{T}}$ and its mirror image at $\boldsymbol{P}\boldsymbol{r}^{(i)} = \left(x^{(i)},\ y^{(i)},\ -z^{(i)} \right)^{\mathrm{T}}$, where $\boldsymbol{P} = \boldsymbol{I} - 2\hat{\boldsymbol{z}}\hat{\boldsymbol{z}}$ is a reflection operator reversing the sign of z-component; $\boldsymbol{S}\left(\boldsymbol{r}\right)$ has the following expression:

$$\boldsymbol{S}\left(\boldsymbol{r}-\boldsymbol{r}^{(i)}\right) = \boldsymbol{S}_0\left(\boldsymbol{r}-\boldsymbol{r}^{(i)}\right) + \boldsymbol{S}_0\left(\boldsymbol{r}-\boldsymbol{P}\boldsymbol{r}^{(i)}\right)\boldsymbol{P}, \tag{S3}$$

where

$$\boldsymbol{S}_0\left(\boldsymbol{r}\right) = \frac{1}{8\pi\eta}\frac{\left(\left|\boldsymbol{r}\right|^2+2\epsilon^2\right)\boldsymbol{I}+\boldsymbol{r}\boldsymbol{r}}{\left(\left|\boldsymbol{r}\right|^2+\epsilon^2\right)^{3/2}}$$

is a regularized Oseen tensor with a regularization parameter ϵ [8, 9]. Setting $\boldsymbol{r} = \boldsymbol{r}^{(i)}$ in Eq. (S2), we can compute flow $\boldsymbol{v}\left(\boldsymbol{r}^{(i)}\right)$ at the location of force $\boldsymbol{f}^{(i)}$ on the cell surface. Because of no-slip boundary condition, $\boldsymbol{v}\left(\boldsymbol{r}^{(i)}\right)$ can also be determined by the swimmer motion:

$$\boldsymbol{v}\left(\boldsymbol{r}^{(i)}\right) = \boldsymbol{v}_{\mathrm{c}} + \boldsymbol{\omega}\times\left(\boldsymbol{r}^{(i)}-\boldsymbol{r}_{\mathrm{c}}\right) + \boldsymbol{v}_{\mathrm{s}}^{(i)},$$

where $\boldsymbol{r}_{\mathrm{c}}$ is the centroid of the swimmer, $\boldsymbol{v}_{\mathrm{c}}$ and $\boldsymbol{\omega}$ are linear and rotational velocities of the swimmer, and the swimming stroke $\boldsymbol{v}_{\mathrm{s}}^{(i)}$ is the velocity of surface elements in the body-fixed frame. Combining these two expressions for $\boldsymbol{v}\left(\boldsymbol{r}^{(i)}\right)$, we have

$$\sum_{j=1}^{N} \boldsymbol{S}\left(\boldsymbol{r}^{(i)}-\boldsymbol{r}^{(j)}\right)\boldsymbol{f}^{(j)} = \boldsymbol{v}_{\mathrm{c}} + \boldsymbol{\omega}\times\left(\boldsymbol{r}^{(i)}-\boldsymbol{r}_{\mathrm{c}}\right) + \boldsymbol{v}_{\mathrm{s}}^{(i)}. \tag{S4}$$

Eq. (S4) gives us $3N$ linear equations for $3N+6$ unknowns: $\boldsymbol{f}^{(i)}$,$\boldsymbol{v}_{\mathrm{c}}$ and $\boldsymbol{\omega}$. To close the system, we use the following (six) constraints of force and torque balances

$$\sum_{i=1}^{N} \boldsymbol{f}^{(i)} = \boldsymbol{0}, \tag{S5}$$

$$\sum_{i=1}^{N} \left(\boldsymbol{r}^{(i)}-\boldsymbol{r}_{\mathrm{c}}\right)\times\boldsymbol{f}^{(i)} = \boldsymbol{0}. \tag{S6}$$

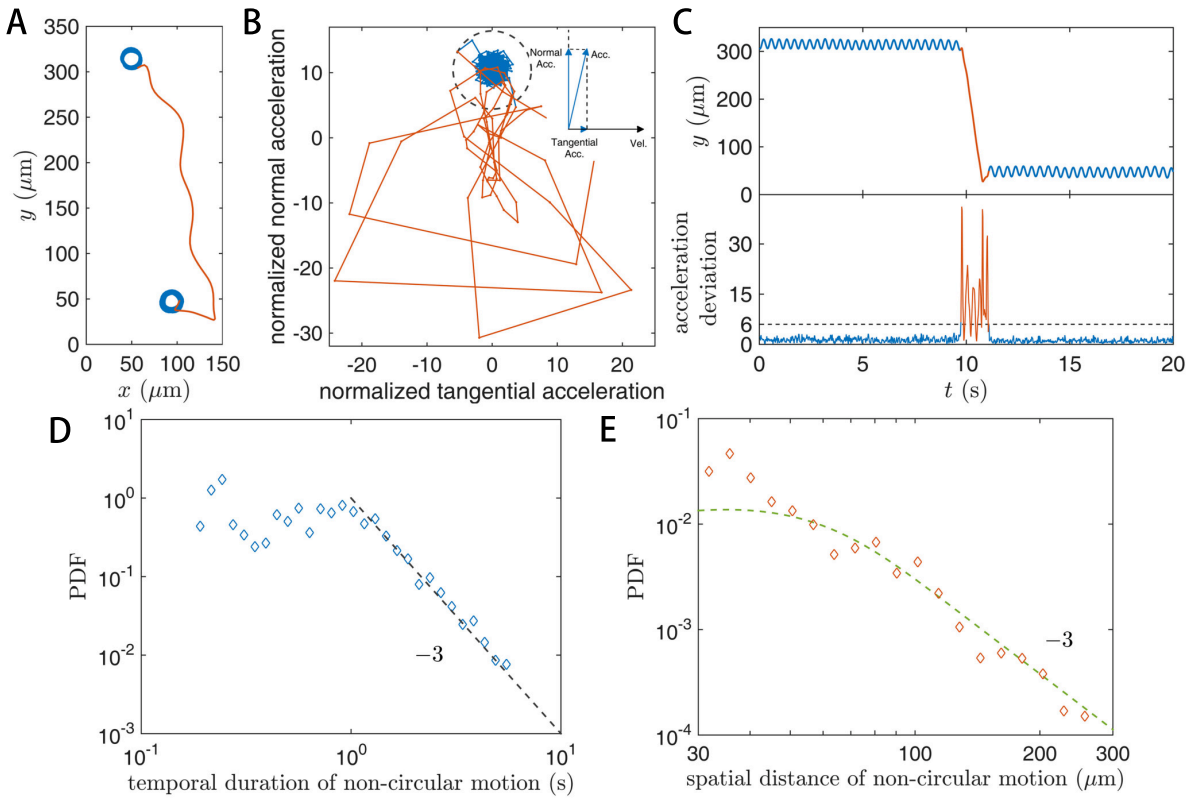

Figure S5. A trajectory containing circular (blue) and non-circular (orange) motion in real space (A) and in phase plane of normal and tangential acceleration components (B). Dashed circle represents a threshold used to separate circular and non-circular motion, see SI text for details. (C) Temporal record of y-coordinate and acceleration deviation of cell motion in (A). (D-E) Probability distributions of temporal duaration and spatial distance of non-circular motion. Green dashed line in (E) represents simulation results with model parameters corresponding to cell density of 198 mm^{-2} in Table SIII.

Eqs. (S4-S6) form a closed linear system from which $\boldsymbol{f}^{(i)}$, $\boldsymbol{v}_{\mathrm{c}}$, and $\boldsymbol{\omega}$ can be solved. Each quantity is linearly related to swimming stroke $\boldsymbol{v}_{\mathrm{s}}$. We denote these linear relations as

$$\boldsymbol{M}^{f}\boldsymbol{v}_{\mathrm{s}} = \boldsymbol{f}, \tag{S7}$$
$$\boldsymbol{M}^{v}\boldsymbol{v}_{\mathrm{s}} = \boldsymbol{v}_{\mathrm{c}}, \tag{S8}$$
$$\boldsymbol{M}^{\omega}\boldsymbol{v}_{\mathrm{s}} = \boldsymbol{\omega}, \tag{S9}$$

where force vector $\boldsymbol{f} \equiv \begin{pmatrix} \boldsymbol{f}^{(1)} \\ \vdots \\ \boldsymbol{f}^{(N)} \end{pmatrix}$, stroke velocity vector $\boldsymbol{v}_{\mathrm{s}} \equiv \begin{pmatrix} \boldsymbol{v}_{\mathrm{s}}^{(1)} \\ \vdots \\ \boldsymbol{v}_{\mathrm{s}}^{(N)} \end{pmatrix}$, $\boldsymbol{M}^{f}$, $\boldsymbol{M}^{v}$ and $\boldsymbol{M}^{\omega}$ are matrices.

After localized forces are obtained from Eq. (S7), we can compute flow velocity ($\boldsymbol{u}$) at any given positions via Eq. (S2):

$$\boldsymbol{S}^{u}\boldsymbol{f} = \boldsymbol{S}^{u}\boldsymbol{M}^{f}\boldsymbol{v}_{\mathrm{s}} = \boldsymbol{u}, \tag{S10}$$

where $\boldsymbol{S}^{u}$ is the regularized Stokeslets matrix depending on the location of interest and $\boldsymbol{r}^{(i)}$.

B. Infer swimming stroke from experimental measurements

Eqs. (S8-S10) establish linear relations that connect swimming stroke $\boldsymbol{v}_{\mathrm{s}}$ to swimmer motion ($\boldsymbol{v}_{\mathrm{c}}$ and $\boldsymbol{\omega}$) and generated flow field ($\boldsymbol{u}$). We use these relations to infer unknown part of the swimming stroke (transverse flagellum, cf. Fig. 1A) from swimmer motion ($\boldsymbol{v}_{\mathrm{c}}$ and $\boldsymbol{\omega}$) and measured flow field ($\boldsymbol{u}$, only the in-plane component of flow field) in Fig. 2A.

To do that, we first discretize the swimmer surface. As shown in Fig. 2C, the longitudinal flagellum is represented by a string of $N_{\mathrm{f}} = 18$ stokeslets and there are $N_{\mathrm{b}} = 700$ stokeslets uniformly covering the spherical cell surface to model the effect of the transverse flagellum. On sphere, distance between nearest surface elements is about 0.65 μm; meanwhile regularization parameter ϵ is chosen to be 0.25 μm. Velocities of these Stokeslets, relative to the center of spherical swimmer body, define the

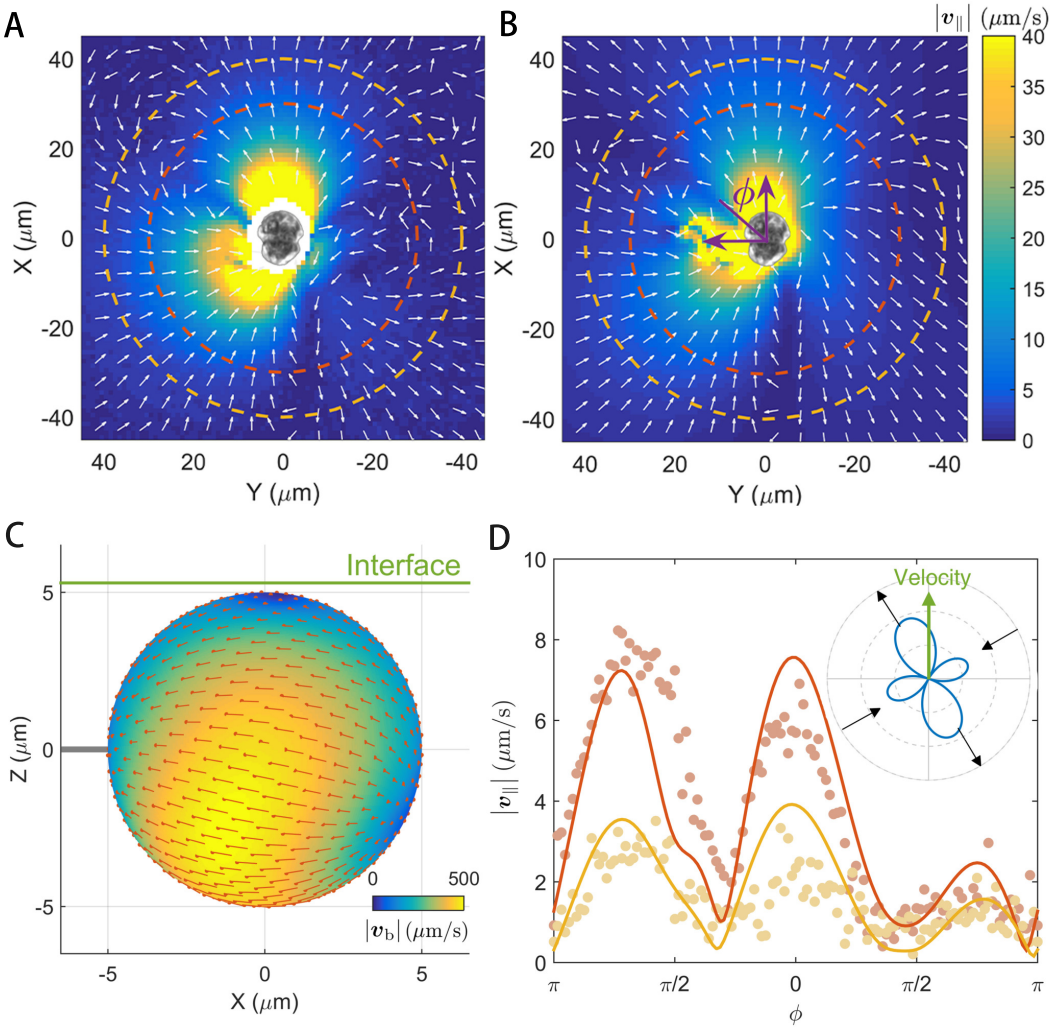

Figure S6. Mean in-plane flow field measured in experiment (A) and regularized Stokeslet model (B). Cell symmetry axis is oriented along the X axis and an angle from X direction is defined as ϕ in (B). (C) An optimal slip flow pattern obtained from our numerical procedure (see Text for details). The air-liquid interface is shown by a green line. (D) Angular dependence of the magnitude of the in-plane velocity at two radii, 30 μm and 40 μm dashed lines in (A) and (B), from experiments (symbols) and numerics (lines). Angular dependence of far-field flow speed (at the radius of 2000 μm, computed from regularized Stokeslet calculation) is shown in the inset; the far-field flow is dominated by a pair of orthogonal pusher-puller dipoles (see SI for detail). Experimental data are measured from tracer motion around a cell with a swimming speed 197 μm/s and a radius 8.8 μm .

swimming stroke $\boldsymbol{v}_{\rm s} = \begin{pmatrix} \boldsymbol{v}_{\rm b} \\ \boldsymbol{v}_{\rm f} \end{pmatrix}$:

$$\boldsymbol{v}_{\rm b} \equiv \begin{pmatrix} \boldsymbol{v}_{\rm b}^{(1)} \\ \vdots \\ \boldsymbol{v}_{\rm b}^{(N_{\rm b})} \end{pmatrix} \equiv \begin{pmatrix} \boldsymbol{v}_{\rm s}^{(1)} \\ \vdots \\ \boldsymbol{v}_{\rm s}^{(N_{\rm b})} \end{pmatrix},$$

$$\boldsymbol{v}_{\rm f} \equiv \begin{pmatrix} \boldsymbol{v}_{\rm f}^{(1)} \\ \vdots \\ \boldsymbol{v}_{\rm f}^{(N_{\rm f})} \end{pmatrix} \equiv \begin{pmatrix} \boldsymbol{v}_{\rm s}^{(N_{\rm b}+1)} \\ \vdots \\ \boldsymbol{v}_{\rm s}^{(N)} \end{pmatrix},$$

where the longitudinal flagellum motion $\boldsymbol{v}_{\rm f}$ can be measured experimentally but the slip flow pattern on cell body $\boldsymbol{v}_{\rm b}$ is unknown (see main text). To get explicit equations for $\boldsymbol{v}_{\rm b}$, we need to rewrite Eq. (S8), Eq. (S9), and Eq. (S10) . Starting with Eq. (S8), we partition $\boldsymbol{M}^v$ into two blocks $\begin{pmatrix} \boldsymbol{M}_{\rm b}^v & \boldsymbol{M}_{\rm f}^v \end{pmatrix}$ and re-write this equation:

$$\boldsymbol{M}^v \boldsymbol{v}_{\rm s} = \begin{pmatrix} \boldsymbol{M}_{\rm b}^v & \boldsymbol{M}_{\rm f}^v \end{pmatrix} \begin{pmatrix} \boldsymbol{v}_{\rm b} \\ \boldsymbol{v}_{\rm f} \end{pmatrix} = \boldsymbol{M}_{\rm b}^v \boldsymbol{v}_{\rm b} + \boldsymbol{M}_{\rm f}^v \boldsymbol{v}_{\rm f} = \boldsymbol{v}_{\rm c}. \tag{S11}$$

Similarly, partitioning $\boldsymbol{M}^\omega$ in Eq. (S9) into blocks $\begin{pmatrix} \boldsymbol{M}_{\rm b}^\omega & \boldsymbol{M}_{\rm b}^\omega \end{pmatrix}$ leads to

$$\boldsymbol{M}_{\rm b}^\omega \boldsymbol{v}_{\rm b} + \boldsymbol{M}_{\rm f}^\omega \boldsymbol{v}_{\rm f} = \boldsymbol{\omega}. \tag{S12}$$

After partitioning $\boldsymbol{M}^f$ into $\begin{pmatrix} \boldsymbol{M}_{\rm b}^f & \boldsymbol{M}_{\rm f}^f \end{pmatrix}$, we rewrite

(S10) as

$$\boldsymbol{S}^u \boldsymbol{f} = \boldsymbol{S}^u \boldsymbol{M}^f \boldsymbol{v}_\mathrm{s} = \boldsymbol{S}^u \boldsymbol{M}^f_\mathrm{b} \boldsymbol{v}_\mathrm{b} + \boldsymbol{S}^u \boldsymbol{M}^f_\mathrm{f} \boldsymbol{v}_\mathrm{f} = \boldsymbol{u}. \quad \text{(S13)}$$

A fourth constraint equation for $\boldsymbol{v}_\mathrm{b}$ arises from non-penetrative boundary condition on the sphere surface:

$$\boldsymbol{K} \boldsymbol{v}_\mathrm{b} = \boldsymbol{0}, \quad \text{(S14)}$$

with

$$\boldsymbol{K} = \begin{pmatrix} \left(\boldsymbol{r}^{(1)} - \boldsymbol{r}_\mathrm{c}\right)^\mathrm{T} & & \\ & \ddots & \\ & & \left(\boldsymbol{r}^{(N_\mathrm{b})} - \boldsymbol{r}_\mathrm{c}\right)^\mathrm{T} \end{pmatrix},$$

a $N_\mathrm{b} \times 3N_\mathrm{b}$ diagonal matrix.

We seek $\boldsymbol{v}_\mathrm{b}$ to satisfy four constraints, Eqs. (S11-S14), which can be written in the following form

$$\begin{pmatrix} \boldsymbol{M}^v_\mathrm{b} \\ \boldsymbol{M}^\omega_\mathrm{b} \\ \boldsymbol{S}^u \boldsymbol{M}^f_\mathrm{b} \\ \boldsymbol{K} \end{pmatrix} \boldsymbol{v}_\mathrm{b} = \begin{pmatrix} \boldsymbol{v}_\mathrm{c} - \boldsymbol{M}^v_\mathrm{f} \boldsymbol{v}_\mathrm{f} \\ \boldsymbol{\omega} - \boldsymbol{M}^\omega_\mathrm{f} \boldsymbol{v}_\mathrm{f} \\ \boldsymbol{u} - \boldsymbol{S}^u \boldsymbol{M}^f_\mathrm{f} \boldsymbol{v}_\mathrm{f} \\ \boldsymbol{0} \end{pmatrix}, \quad \text{(S15)}$$

or in a compact form as

$$\boldsymbol{A} \boldsymbol{v}_\mathrm{b} = \boldsymbol{b}, \quad \text{(S16)}$$

with $\boldsymbol{A} = \begin{pmatrix} \boldsymbol{M}^v_\mathrm{b} \\ \boldsymbol{M}^\omega_\mathrm{b} \\ \boldsymbol{S}^u \boldsymbol{M}^f_\mathrm{b} \\ \boldsymbol{K} \end{pmatrix}$ and $\boldsymbol{b} = \begin{pmatrix} \boldsymbol{v}_\mathrm{c} - \boldsymbol{M}^v_\mathrm{f} \boldsymbol{v}_\mathrm{f} \\ \boldsymbol{\omega} - \boldsymbol{M}^\omega_\mathrm{f} \boldsymbol{v}_\mathrm{f} \\ \boldsymbol{u} - \boldsymbol{S}^u \boldsymbol{M}^f_\mathrm{f} \boldsymbol{v}_\mathrm{f} \\ \boldsymbol{0} \end{pmatrix}$.

As shown in Fig. 2*A*, measured in-plane velocity field $\boldsymbol{u}$ is experimentally measured on a grid with 3200 points. Therefore, Eq. (S16) represents 7106 [3(cell velocity)+3(cell angular velocity)+3200 × 2(two components of $\boldsymbol{u}$ field)+700(non-penetrative boundary condition)] linear equations for 2100 (3 × 700) unknowns ($\boldsymbol{v}_\mathrm{b}$). To solve this over-constrained linear problem, we used Moore-Penrose inverse:

$$\boldsymbol{v}_\mathrm{b} = \boldsymbol{A}^+(t)\, \boldsymbol{b},$$

where $\boldsymbol{A}^+(t)$ is Moore-Penrose inverse of $\boldsymbol{A}$ with a tolerance t. Moore-Penrose inverse is a kind of pseudo-inverse based on singular value decomposition. We empirically choose the tolerance value in Moore-Penrose inverse algorithm to be the 714th singular value of $\boldsymbol{A}$. With tolerance around the chosen value, the algorithm produces excellent fits for the flow field and smooth slip-flow pattern on the sphere, as shown by results in Fig. 2 and Fig. S6.

C. Stalled force and torque generated by flagella

We use the Regularized Stokeslet method to compute contributions of two flagella to stalled force and torque. For that, we set cell translation and rotation velocities to be zero, $\boldsymbol{v}_\mathrm{c} = \boldsymbol{0}$ and $\boldsymbol{\omega} = \boldsymbol{0}$, and Eq. (S4) becomes

$$\sum_{j=1}^{N} \boldsymbol{S}\left(\boldsymbol{r}^{(i)} - \boldsymbol{r}^{(j)}\right) \boldsymbol{f}^{(j)} = \boldsymbol{v}^{(i)}_\mathrm{s},$$

which can also be denoted as

$$\boldsymbol{S}\boldsymbol{f} = \boldsymbol{v}_\mathrm{s} = \begin{pmatrix} \boldsymbol{v}_\mathrm{b} \\ \boldsymbol{v}_\mathrm{f} \end{pmatrix}.$$

Forces that the cell acts on fluid can be solved out

$$\boldsymbol{f} \equiv \begin{pmatrix} \boldsymbol{f}_\mathrm{b} \\ \boldsymbol{f}_\mathrm{f} \end{pmatrix} = \boldsymbol{S}^{-1} \begin{pmatrix} \boldsymbol{v}_\mathrm{b} \\ \boldsymbol{v}_\mathrm{f} \end{pmatrix},$$

where $\boldsymbol{f}_\mathrm{b}$ and $\boldsymbol{f}_\mathrm{f}$ are forces generated by transverse and longitudinal flagellum, respectively. From $\boldsymbol{f}_\mathrm{b}$ and $\boldsymbol{f}_\mathrm{f}$, we can compute total force and torque contributions by two flagella; results are shown in in Table SI.

		transverse	longitudinal	total
force (pN)	X	14.4	−1.1	13.3
	Y	−1.2	−0.5	−1.7
	Z	−0.4	0.3	−0.1
torque (μm · pN)	X	−2.6	1.5	−1.1
	Y	−0.4	−1.1	−1.5
	Z	73.8	29.4	103.2

Table SI. Stalled force and torque contributions from two sets of flagella.

D. Far-field flow scaling in the cell plane

We focus on fluid flow in the horizontal plane where cell centers are, cf. Fig. 2*B* . In Fig. S7, we plot angular profiles of radial and tangential velocity components at the radius $r = 1000$ μm calculated by Eq. (S10); such profiles can be decomposed into low-order Fourier components. After carrying out similar Fourier analysis on profiles at different radius, we found that coefficients for Fourier components decay with radius r in power laws and we can parameterize the far-field flow as

$$\frac{V^\mathrm{far}_\mathrm{r}(r,\phi)}{v_\mathrm{c}} \approx A_0 \frac{\cos(\phi - \psi_0)}{r^3} + A_{11} \frac{3\cos(\phi - \psi_1)^2 - 1}{r^2} + A_{12} \frac{3\sin(\phi - \psi_1)^2 - 1}{r^2}, \quad \text{(S17)}$$

$$\frac{V^\mathrm{far}_\mathrm{t}(r,\phi)}{v_\mathrm{c}} \approx B_0 \frac{1}{r^4} + B_1 \frac{\sin(\phi - \xi_1)}{r^3} + B_2 \frac{\sin 2(\phi - \xi_2)}{r^4} + B_3 \frac{\sin 3(\phi - \xi_3)}{r^3} + B_4 \frac{\sin 4(\phi - \xi_4)}{r^4}. \quad \text{(S18)}$$

Parameter values for Fourier coefficients and phase are listed in Table SII. In Eq. (S17) , A_{11} and A_{12} terms represent two perpendicular force-dipoles and A_0 term represents a mixed contribution of source-dipole and force-quadrupole; force-dipole terms dominate in the far field, as shown in the insets of Fig. 2*D* and Fig. S6*D*. In Eq. (S18) , B_0 term represents contributions from a pair of rotlet-dipole.

We average Eqs. (S17) and (S18) along a circular trajectory of radius a, cf. Fig. 5*A* and obtain the following expressions for period-averaged flow in far field:

$$\frac{\bar{V}_R^{\text{far}}(R)}{v_c} = \frac{A_{11}+A_{12}}{2R^2} + \mathrm{O}\left(\frac{1}{R^3}\right), \tag{S19}$$

$$\begin{aligned}\frac{\bar{V}_\varphi^{\text{far}}(R)}{v_c} =& A_0\frac{a\cos\psi_0}{2R^4} + (-A_{11}+A_{12})\frac{3a^2\sin 2\psi_1}{8R^4} \\ &+ B_0\frac{1}{R^4} - B_1\frac{a\cos\xi_1}{R^4} + \mathrm{O}\left(\frac{1}{R^5}\right).\end{aligned} \tag{S20}$$

Using parameters in Table SI and setting $a = 10$ μm, we find that Eq. (S20) is dominated by A_0 term. Therefore, we can rewrite the far-field flow as

$$\bar{\boldsymbol{V}}^{\text{far}}(\boldsymbol{R}; v_c) = v_c\left(\frac{p}{R}\right)^2\hat{\boldsymbol{R}} + v_c\left(\frac{q}{R}\right)^4\hat{\boldsymbol{\varphi}}, \tag{S21}$$

where we have

$$\begin{aligned} p &\equiv \left(\frac{A_{11}+A_{12}}{2}\right)^{1/2} = 1.664\ \mu\text{m}, \\ q &\equiv \left(A_0\frac{a\cos\psi_0}{2}\right)^{1/4} = 7.999\ \mu\text{m}. \end{aligned}$$

As for the full data of period-averaged flow from $R = 30$ to 2000 μm shown in Fig. 5*A*, they can be well fitted by adding higher order terms to Eq. (S21), which are

$$\begin{aligned} \bar{V}_R(R) &= v_c\left(\frac{1.646\ \mu\text{m}}{R}\right)^2 + v_c\left(\frac{3.269\ \mu\text{m}}{R}\right)^3, \\ \bar{V}_\varphi(R) &= v_c\left(\frac{7.733\ \mu\text{m}}{R}\right)^4 + v_c\left(\frac{6.688\ \mu\text{m}}{R}\right)^5; \end{aligned} \tag{S22}$$

these formulas can be used for the calculation of interaction in the simulation, as shown in Fig. S12.

III. MEAN FLOW AROUND A SPINNING FORCE DIPOLE

In this subsection, we calculate the average flow field generated by a force dipole that lies and spins in the x-y plane. For that, let us first consider a force dipole locating at the origin and pointing at z-axis; the dipole

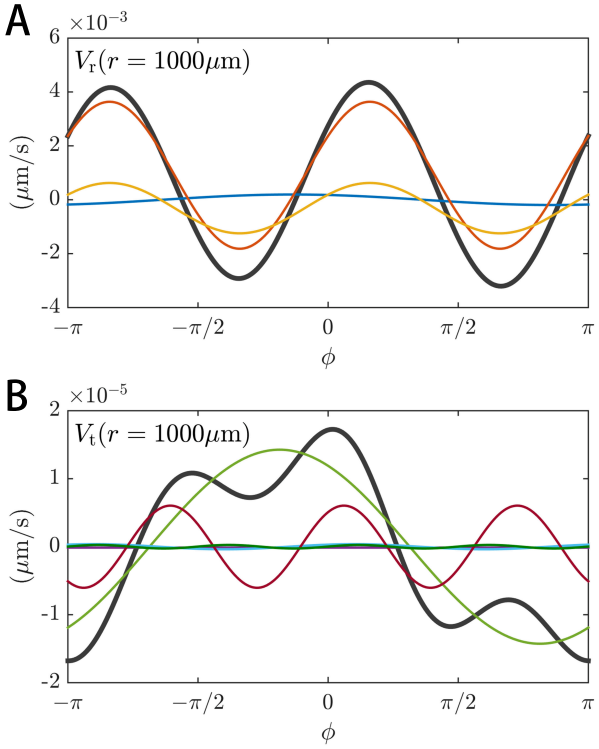

Figure S7. Analysis of instantaneous flow field in the far field. Fourier decomposition of radial (A) and tangential (B) components at the radius $r = 1000$ μm. Thick black lines are results from the regularized Stokeslet method and thin colored lines are Fourier components in Eq. (S17) and Eq. (S18).

A_0	-900.4	μm^3	ψ_0	-0.4291
A_{11}	8.419	μm^2	ψ_1	0.5032
A_{12}	-2.885	μm^2		
B_0	-6.9	μm^4		
B_1	-66.07	μm^3	ξ_1	0.9855
B_2	$1736.$	μm^4	ξ_2	-0.4741
B_3	27.99	μm^3	ξ_3	-0.3337
B_4	$1204.$	μm^4	ξ_4	-0.0210

Table SII. Values for coefficient of Fourier components in Eq. (S17) and Eq. (S18)

generates flow field as

$$\begin{aligned}\boldsymbol{u}(\boldsymbol{r}) &= \frac{p}{r^2}\left(3\cos^2\theta - 1\right)\hat{\boldsymbol{r}}, \\ &= \frac{p}{(x^2+y^2+z^2)^{3/2}}\left(3\frac{z^2}{x^2+y^2+z^2} - 1\right)\begin{pmatrix}x\\y\\z\end{pmatrix},\end{aligned} \tag{S23}$$

where θ is the polar angle between $\boldsymbol{r}$ and z-axis. We next introduce a rotation operation $\boldsymbol{O}(\xi)$ rotating the dipole

direction from the z-axis to the x-y plane, pointing at $\left(\cos\xi,\ \sin\xi,\ 0\right)^{\mathrm{T}}$:

$$\begin{aligned}\boldsymbol{O}(\xi) &= \boldsymbol{O}\left(\hat{\boldsymbol{z}} \to \left(\cos\xi,\ \sin\xi,\ 0\right)^{\mathrm{T}}\right) \\ &= \boldsymbol{O}\left(\hat{\boldsymbol{x}} \to \left(\cos\xi,\ \sin\xi,\ 0\right)^{\mathrm{T}}\right) \boldsymbol{O}\left(\hat{\boldsymbol{z}} \to \hat{\boldsymbol{x}}\right) \\ &= \begin{pmatrix} \cos\xi & -\sin\xi & 0 \\ \sin\xi & \cos\xi & 0 \\ 0 & 0 & 1 \end{pmatrix} \begin{pmatrix} 0 & 0 & 1 \\ 0 & 1 & 0 \\ -1 & 0 & 0 \end{pmatrix} \\ &= \begin{pmatrix} 0 & -\sin\xi & \cos\xi \\ 0 & \cos\xi & \sin\xi \\ -1 & 0 & 0 \end{pmatrix}.\end{aligned}$$

Applying the rotation operation $\boldsymbol{O}(\xi)$ to the initial flow field $\boldsymbol{u}(\boldsymbol{r})$ in Eq. S(S23), we arrive at the flow field:

$$\boldsymbol{u}'(\boldsymbol{r};\xi) = \left[\boldsymbol{O}(\xi)\,\boldsymbol{u}\right](\boldsymbol{r}) = \boldsymbol{O}(\xi)\,\boldsymbol{u}\left(\boldsymbol{O}(\xi)^{-1}\,\boldsymbol{r}\right).$$

Averaging the above expression over the orientation ξ, we obtain the period-average flow:

$$\begin{aligned}\bar{\boldsymbol{u}}(\boldsymbol{r}) &= \frac{1}{2\pi}\int_{-\pi}^{\pi} \boldsymbol{u}'(\boldsymbol{r};\xi)\,\mathrm{d}\xi \\ &= -\frac{p}{2r^2}\left(3\cos^2\theta - 1\right)\hat{\boldsymbol{r}} = -\frac{1}{2}\boldsymbol{u}(\boldsymbol{r}),\end{aligned} \tag{S24}$$

a dipolar field with a reduced strength from that in Eq. (S23). This result can be used to understand period-average 3D flow around a circling cell in Fig. S8, which shows a force dipole scaling in the far-field.

$\rho\ (\mathrm{mm}^{-2})$	41	77	198	369
T (s)	1600	300	400	300
$D_0\ (\mu\mathrm{m}^2/\mathrm{s})$	1.05	0.65	0.95	0.96

Table SIII. Optimized model parameters (T and D_0) at four cell densities (ρ).

IV. DESCRIPTION OF MOVIES

Movie S1: Holographic movie of a cell approaching and adhering to the air-liquid interface.

Movie S2: Cell and flagellar motion in the laboratory (left) and cell-body(right) frames at the air-liquid interface.

Movie S3: Tracer motion around a circularly swimming cell at the air-liquid interface.

Movie S4-5: Hyperuniform states of cells at two densities: 41 mm^{-2} and 369 mm^{-2}. Imaging window size is 1.6 mm. Examples of circular and non-circular trajectories are shown by blue and red lines, respectively.

[1] H. J. Jeong, S. Y. Lee, N. S. Kang, Y. Du Yoo, A. S. Lim, M. J. Lee, H. S. Kim, W. Yih, H. Yamashita, and T. C. LaJeunesse, "Genetics and morphology characterize the dinoflagellate symbiodinium voratum, n. sp., (dinophyceae) as the sole representative of symbiodinium clade e," *Journal of Eukaryotic Microbiology*, vol. 61, no. 1, pp. 75–94, Jan. 2014.

[2] J. Happel and H. Brenner, *Low Reynolds number hydrodynamics: with special applications to particulate media*. Springer Science & Business Media, 1983, vol. 1.

[3] R. Ma, G. S. Klindt, I. H. Riedel-Kruse, F. Julicher, and B. M. Friedrich, "Active phase and amplitude fluctuations of flagellar beating," *Physical Review Letters*, vol. 113, no. 4, p. 048101, Jul. 2014.

[4] K. Y. Wan and R. E. Goldstein, "Rhythmicity, recurrence, and recovery of flagellar beating," *Physical Review Letters*, vol. 113, no. 23, p. 238103, Dec. 2014.

[5] R. E. Goldstein, "Green algae as model organisms for biological fluid dynamics," *Annual Review of Fluid Mechanics, Vol 47*, vol. 47, pp. 343–375, 2015.

[6] R. Cortez, "The method of regularized stokeslets," *SIAM Journal on Scientific Computing*, vol. 23, no. 4, pp. 1204–1225, 2001.

[7] J. Ainley, S. Durkin, R. Embid, P. Boindala, and R. Cortez, "The method of images for regularized stokeslets," *J. Comput. Phys.*, vol. 227, no. 9, pp. 4600–4616, Apr. 2008.

[8] G. Perkins and R. Jones, "Hydrodynamic interaction of a spherical particle with a planar boundary i. free surface," *Physica A-statistical Mechanics and Its Applications*, vol. 171, no. 3, pp. 575–604, 1991.

[9] S. E. Spagnolie and E. Lauga, "Hydrodynamics of self-propulsion near a boundary: predictions and accuracy of far-field approximations," *J. Fluid Mech.*, vol. 700, pp. 105–147, Jun. 2012.

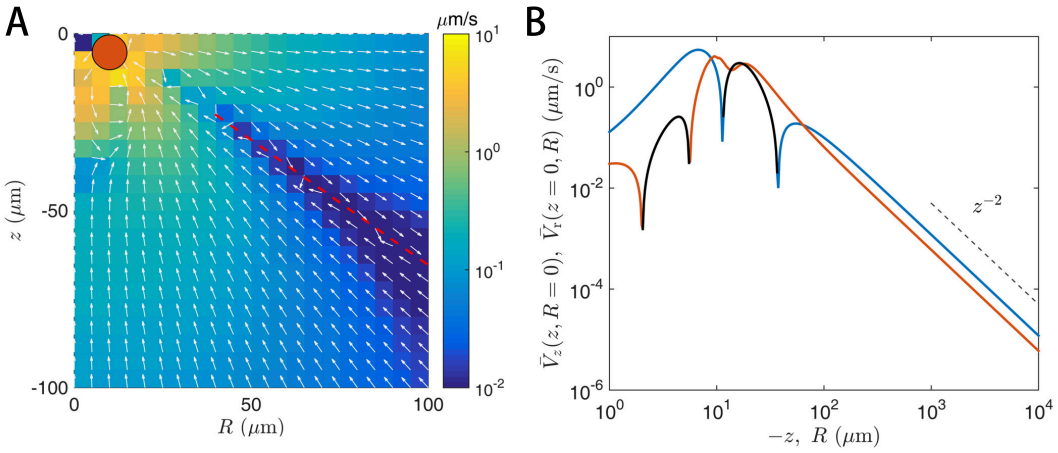

Figure S8. (A) Radial component of period-averaged flow field in R-z plain. Cell, represented by an orange circle, centers at the position ($R = 10$ μm, z $= -5.3$ μm). The air-liquid interface is at $z = 0$. Red dashed line, forming an angle of arccos $\frac{1}{\sqrt{3}}$ to z-axis, roughly marks where flow reverses direction, seen in Eq. (S24). (B) Magnitude of radial component along z- [$V_z\,(z, R = 0)$, blue] and R- [$V_r\,(z = 0, R)$, orange] axis. The ratio of $V_z\,(z, R = 0)$ to $V_r\,(z = 0, R)$ approaches 2 in the far-field, in agreement with Eq. (S24) of $\theta = 0$ to $\pi/2$.

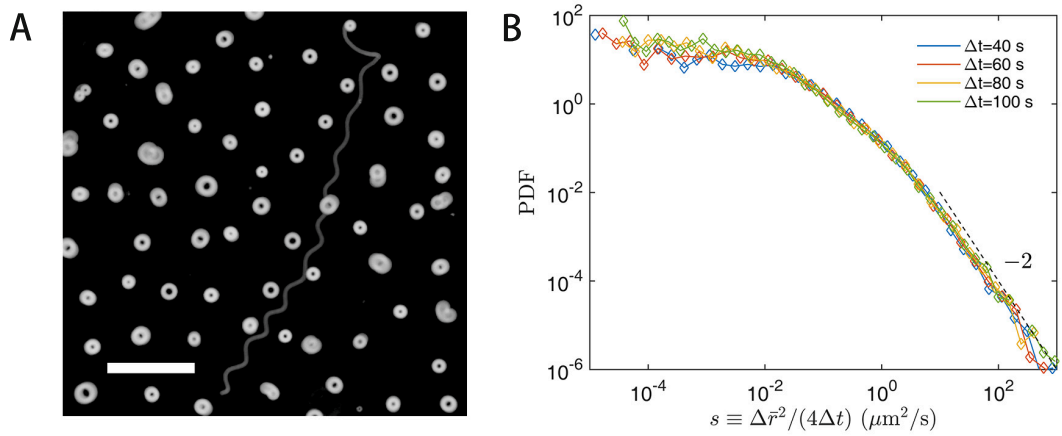

Figure S9. (A) Streak image of cell motion. Raw images are obtained at cell density 77 mm^{-2} and averaged over 10 sec to produce the streak image. Scale bar is 200 μm. (B) Probability distribution functions of averaged cell displacements from experiment. See Fig. 3 for similar results obtained from another cell.

X, Y, Z	coordinates in cell-body frame
x, y, z	coordinates in lab frame
a, ω, v_c	radius, angular velocity, and linear speed of cell circular motion
$\boldsymbol{r}(t)$	instantaneous cell position
$\bar{\boldsymbol{r}}(t)$	window-averaged (2 s) cell position
ρ	global cell number density
$\delta\rho$	standard deviation of local cell number density
L	size of square window used to measure density fluctuations
$S(k)$	static structure factor
$\bar{\boldsymbol{V}}$	period-averaged flow field produced by a circularly swimming cell
$\boldsymbol{R}$	position vector respecting to the center of cell circular trajectory
R, φ	radius and azimuth angle of $\boldsymbol{R}$ vector
T	mean stationary time of circular motion
D	cell diffusivity due to stochastic non-circular motion
D_0	cut-off diffusivity in cell diffusivity distribution
β	power index in cell diffusivity distribution
$\boldsymbol{\eta}$	random displacements representing stochastic non-circular motion
τ	time step in simulation
$L_{\max}$	size of computational domain
R_{cell}	average radius of cell body
l	average distance from the center of a circularly-swimming cell to air-liquid interface
$\boldsymbol{r}_{\text{c}}$	position of cell center used in the regularized Stokeslet model
$\boldsymbol{f}$	localized force in the regularized Stokeslet model
$\boldsymbol{S}$	Green's function in the regularized Stokeslet model
$\boldsymbol{v}$	flow field produced by localized forces
$\boldsymbol{v}_{//}$	flow field in the plane of cell motion
$\boldsymbol{v}_{\text{s}}$	stroke velocity on the cell surface
$\boldsymbol{v}_{\text{b}}$,$\boldsymbol{v}_{\text{f}}$	components of $\boldsymbol{v}_{\text{s}}$ on cell body and on longitudinal flagellum
$\boldsymbol{f}_{\text{b}}$,$\boldsymbol{f}_{\text{f}}$	components of $\boldsymbol{f}$ on cell body and on longitudinal flagellum
$\boldsymbol{A}^{+}$	Moore-Penrose inverse of $\boldsymbol{A}$
r, ϕ	radius and azimuth angle in polar coordinate used to compute flow in the far field
$V_{\text{r}}^{\text{far}}$, $V_{\text{t}}^{\text{far}}$	radial and tangential components of instantaneous flow in the far field
V_R, V_φ	radial and tangential components of period-averaged flow of a circularly-swimming cell
V_R^{far}, V_φ^{far}	V_{R}, V_φ in the far field

Table SIV. List of symbols in the manuscript

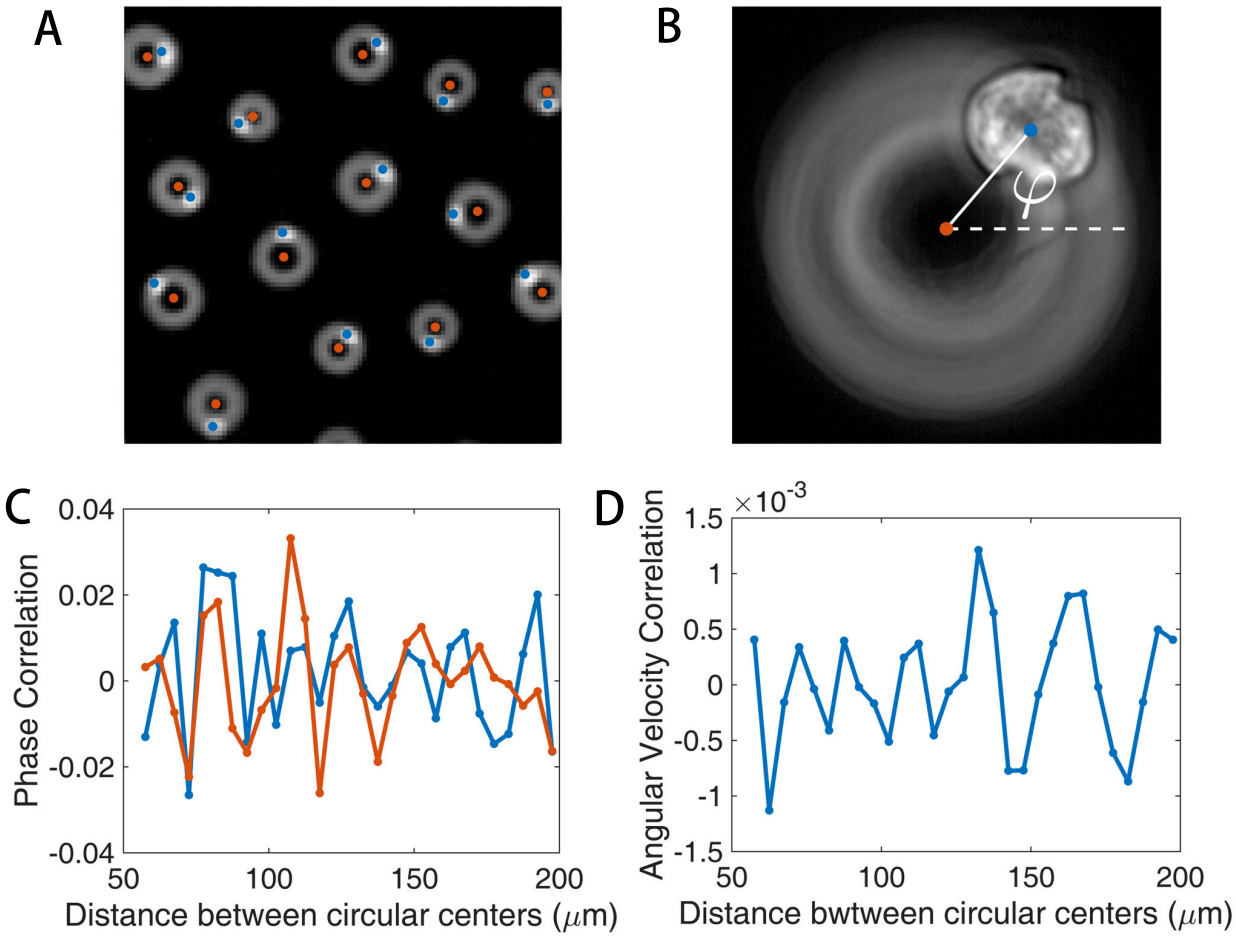

Figure S10. (A) Cell-body centers (blue, $\boldsymbol{r}(t)$) and centers of circular trajectories (orange, $\bar{\boldsymbol{r}}(t)$) marked on the superposition of instantaneous and streak images. Part of A is shown in (B). φ denotes the phase of circular motion. (C) Correlation of circular motion. Polar (blue) and nematic (orange) correlations can be calculated by averaging $\cos\Delta\varphi$ and $\cos 2\Delta\varphi$, with $\Delta\varphi$ the phase difference of two cells at a given distance. (D) Correlation (normalized) of instantaneous angular velocity between a pair of cells.

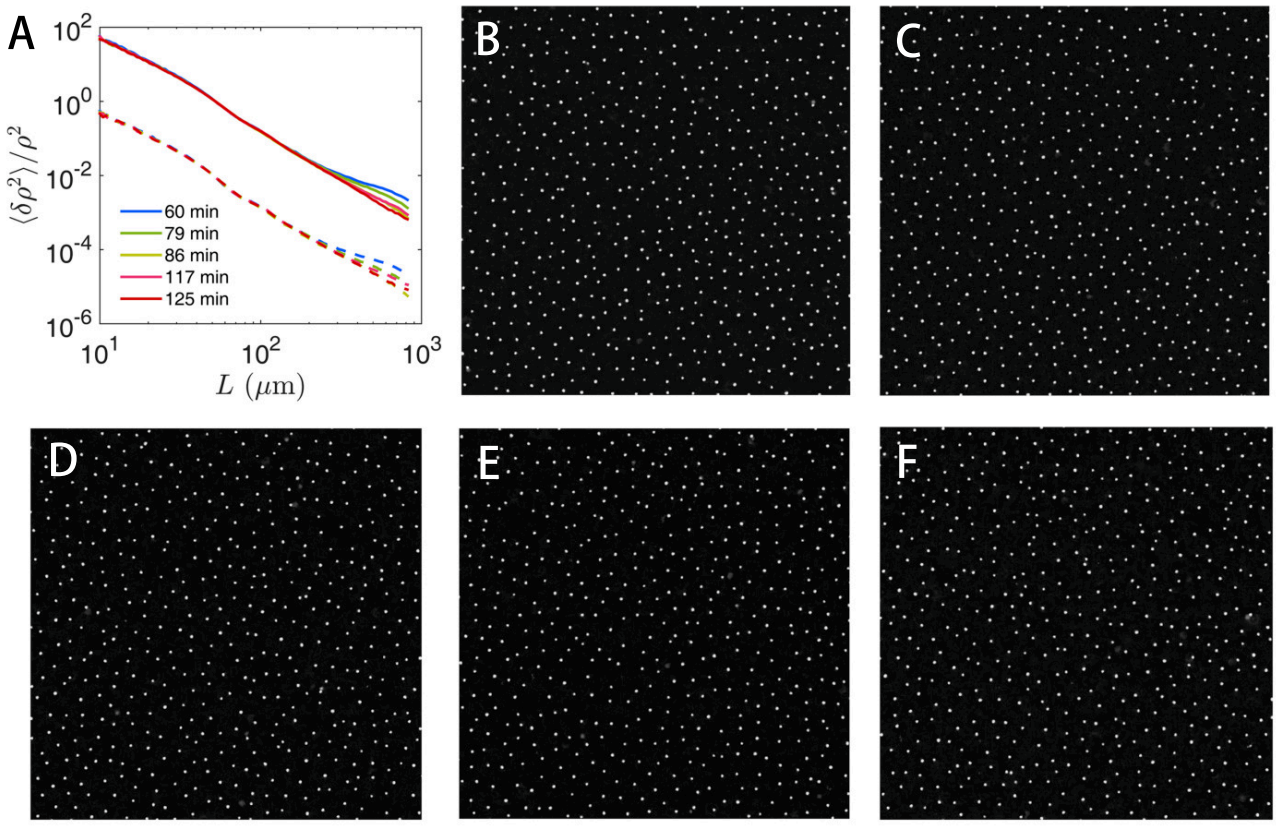

Figure S11. (A) Evolution of density fluctuations computed from instantaneous cell position [$\boldsymbol{r}(t)$, solid lines] and window-averaged position [$\bar{\boldsymbol{r}}(t)$, dashed lines]. For clarity, dashed lines have been decreased by two orders of magnitude. (B-F) Corresponding snapshots at five moments in (A) with a window size of 1.6 mm. Blue line in A corresponds to data measured at 60 minutes after the sample is made.

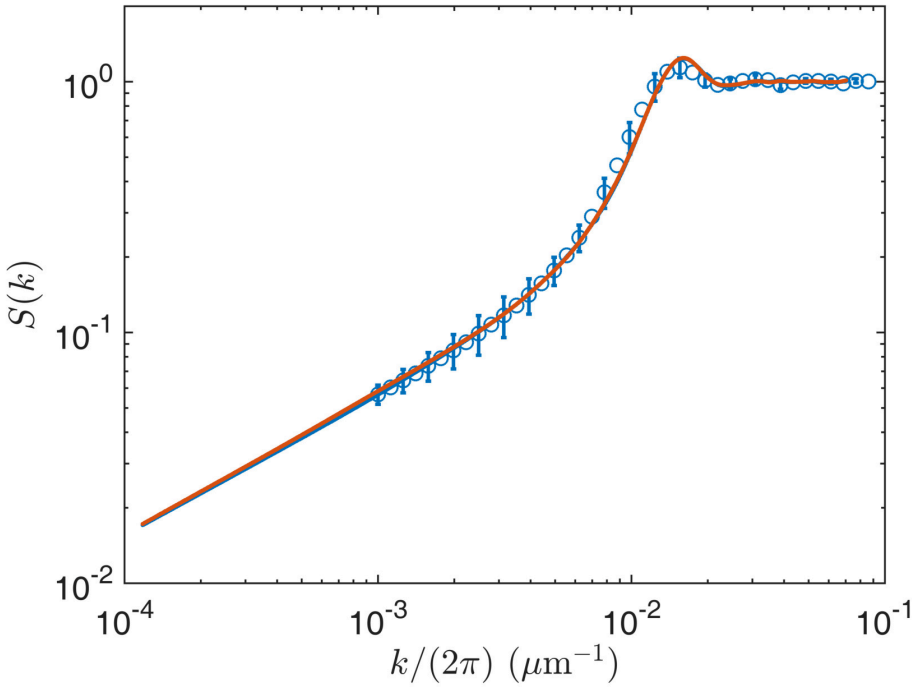

Figure S12. Structure factors computed with interpolated flow [Fig. 5*A*, blue line] and far-field expression [Eq. (S22), red line] in particle-based model. Both approaches generate results in agreement with experimental data (circles).